

DSMC-LBM mapping scheme for rarefied and non-rarefied gas flows

G. Di Staso^{a,*}, H.J.H. Clercx^a, S. Succi^c, F. Toschi^{a,b,c}

^a*Department of Applied Physics, Eindhoven University of Technology,
Den Dolech 2, 5600 MB, Eindhoven, Netherlands*

^b*Department of Mathematics and Computer Science, Eindhoven University of Technology,
Den Dolech 2, 5600 MB, Eindhoven, Netherlands*

^c*Istituto per le Applicazioni del Calcolo, Consiglio Nazionale delle Ricerche,
Via dei Taurini 19, 00185, Rome, Italy*

Abstract

We present the formulation of a kinetic mapping scheme between the Direct Simulation Monte Carlo (DSMC) and the Lattice Boltzmann Method (LBM) which is at the basis of the hybrid model used to couple the two methods in view of efficiently and accurately simulate isothermal flows characterized by variable rarefaction effects. Owing to the kinetic nature of the LBM, the procedure we propose ensures to accurately couple DSMC and LBM at a larger Kn number than usually done in traditional hybrid DSMC—Navier-Stokes equation models. We show the main steps of the mapping algorithm and illustrate details of the implementation. Good agreement is found between the moments of the single particle distribution function as obtained from the mapping scheme and from independent LBM or DSMC simulations at the grid nodes where the coupling is imposed. We also show results on the application of the hybrid scheme based on a simpler mapping scheme for plane Poiseuille flow at finite Kn number. Potential gains in the computational efficiency assured by the application of the coupling scheme are estimated for the same flow.

Keywords: kinetic theory, Grad's moments method, non-equilibrium effects,

*Corresponding author

Email addresses: g.di.staso@tue.nl, +31 40 247 21 43 (G. Di Staso),
h.j.h.clercx@tue.nl (H.J.H. Clercx), succi@iac.cnr.it (S. Succi), f.toschi@tue.nl (F. Toschi)

1. Introduction

Research in gas flows characterized by a large range of scales and by disparate levels of non-equilibrium effects poses a challenge to statistical physics modelling and rises interest in industry for simulating flows in micro-, nano-electromechanical systems and in material processing tools [1–3]. The extent of the departure of a flow from the equilibrium state is traditionally measured in terms of the Knudsen number:

$$\text{Kn} = \frac{\lambda}{\ell} \approx \frac{\lambda}{Q} \left| \frac{dQ}{d\ell} \right|, \quad (1)$$

where λ is the gas mean free path, ℓ is the smallest hydrodynamic characteristic scale and Q is a fluid dynamic quantity of interest such as the gas pressure, velocity, temperature [4]. According to the Knudsen number, the gas
5 flows can be classified into the hydrodynamic ($\text{Kn} < 0.01$), slip ($0.01 < \text{Kn} < 0.1$), transition ($0.1 < \text{Kn} < 10$) and free molecular regime ($\text{Kn} > 10$). The kinetic description of gases based on the Boltzmann equation, valid at any Kn , allows to cover flow conditions from the very rarefied to the hydrodynamic limit [5]. The two limits, rarefied and continuum, have traditionally been studied nu-
10 merically by approximating the Boltzmann equation via the Direct Simulation Monte Carlo (DSMC) [6] or by solving the Navier-Stokes equations which can be derived from truncation at first order of the Chapman-Enskog procedure [7]. While the DSMC method is particularly suited to rarefied gas flow (transitional regime), its computational costs make it unpractical to study hydrodynamic
15 flows [2]. Conversely, the continuum description of the flow provided by solving the Navier-Stokes equations and applying the no-slip boundary condition is not accurate whenever $\text{Kn} > 0.01$ [8]. Corrections to the boundary conditions of Navier-Stokes equations such as to reproduce the velocity slip and temperature jump at the gas-surface interface in case of slip flow regime are often

20 not accurate and may also predict incorrect qualitative behavior of the flow
 [9, 10]. Moreover, the derivation of extended hydrodynamic equations employ-
 ing higher-order Chapman-Enskog approximations (Burnett and super-Burnett
 equations) have showed limited success [8]. Alternatively, macroscopic trans-
 port equations can be originated from moments expansion methods such as the
 25 Grad’s method [11, 12]. However, difficulties in imposing boundary conditions
 for those moments without a clear physical meaning, as well complexity in the
 resulting systems of equations prevent the application of the method for the
 simulation of flows of industrial interest.

It is therefore evident that whenever the flow presents a large range of Kn , due
 30 to the current computational and modelling limitations of the available meth-
 ods, a multiscale hybrid model has to be used.

When dealing with multiscale models, *domain decomposition techniques* repre-
 sent the most natural way to handle the problem. Within this approach, the
 domain is decomposed according to a continuum breakdown parameter between
 35 regions where continuum-level macroscopic equations (either Euler or Navier-
 Stokes equations) are valid and regions where substantial non-equilibrium effects
 are present and kinetic methods, typically DSMC, are needed (see Refs. [8, 13–
 19]). Then a special treatment is imposed to couple the flow fields in the areas
 of overlap between the different regions, e.g. [20–22].

40 For completeness, the domain decomposition technique is not the only method
 adopted in the literature as alternative approaches are proposed. For example
 in [23], the Boltzmann equation is solved for a short period of time to obtain
 the rate of change of the average flow variables which are then used to update
 the continuum-level velocity field. In [24], instead, macroscopic equations are
 45 modified so to include effects due to kinetic contributions which take into ac-
 count perturbations from the equilibrium state of the velocity distribution.

The approach that we introduce here follows the domain decomposition tech-
 nique as commonly done in models proposed in literature but it departs from
 those as the flow at the continuum level and at moderate rarefied conditions is
 50 simulated with the Lattice Boltzmann Method (LBM).

Moreover, since it has been largely demonstrated that LBM, due to its intrinsic kinetic nature, is an accurate and efficient numerical solver not only for flows at Navier-Stokes description level but also for flows at finite Kn number (see Refs. [25–37]), the present model has the advantage, over the other hybrid methods
55 which use traditional Navier-Stokes solvers, that the need for using the computationally expensive DSMC solver can be postponed to larger values of Kn. This is equivalent to say that the size of the domain where DSMC solver is still needed can be significantly reduced, thus improving the overall computational efficiency of the simulation.

60 In this work we principally focus on the most delicate aspect of any hybrid coupling model, i.e. the two-way extraction and transfer of information at the interface between the two numerical methods. The *mapping* schemes we developed, in fact, allow to pass from DSMC to LBM domains and vice versa correctly transferring also the non-equilibrium information. The *amount* of
65 non-equilibrium information that can be passed is then essentially determined by the LB model and in particular by the chosen set of discrete velocities and the isotropy conditions the set is able to fulfill.

Simulations performed to validate the mapping scheme show that an accurate transfer of information is achievable for flows up to $Kn=0.25$ for a 39-points
70 Gauss-Hermite quadrature with sixth-order isotropy (D3Q39).

Finally, to check functionality of the DSMC-LBM hybrid model and assess its computational efficiency, tests, based on a simpler mapping scheme, are also performed showing, for the particular simulated flow, a significant speed-up with respect to a full DSMC simulation.

75 **2. Mapping schemes**

Since both LB and DSMC are widely documented in the literature, only a few basic aspects are discussed in this paper. For an exhaustive treatment about DSMC and LBM methods, the reader should refer to [6] and [38]. Both methods aim to determine the fluid motion as described by the Boltz-

mann equation. The main feature which clearly distinguishes the LBM from the DSMC, is the reduction of the degrees of freedom of the velocity space. In fact in LBM particles at each lattice site \mathbf{x} can only propagate along a finite number of directions with an assigned speed ξ_a , while in DSMC the velocity space is not constrained to a set of discrete velocities.

Before introducing the mapping scheme between the DSMC and LBM, we note that in order to quantitatively reproduce DSMC solutions for finite-Kn number flows, the LB model needs three basic *ingredients*:

1. kinetic boundary conditions, [37, 39–43];
2. higher-order lattice (HOL), [29, 44];
3. regularization procedure, [29, 45].

The main idea at the basis of the *mapping scheme* is that the single particle distribution function $f(\mathbf{x}, \boldsymbol{\xi}, t)$ can be expanded in terms of the dimensionless Hermite orthonormal polynomials, $\mathcal{H}(\boldsymbol{\xi})$, in the velocity space $\boldsymbol{\xi}$ as [11, 12, 44]:

$$f(\mathbf{x}, \boldsymbol{\xi}, t) = \omega(\boldsymbol{\xi}) \sum_{n=0}^{\infty} \frac{1}{n!} \mathbf{a}^{(n)}(\mathbf{x}, t) \mathcal{H}^{(n)}(\boldsymbol{\xi}), \quad (2)$$

where $\omega(\boldsymbol{\xi})$ is the weight function associated with the Hermite polynomials, and $\mathbf{a}^{(n)}$ are the rank- n tensors representing the dimensionless expansion coefficients defined as:

$$\mathbf{a}^{(n)} = \int f(\mathbf{x}, \boldsymbol{\xi}, t) \mathcal{H}^{(n)}(\boldsymbol{\xi}) d\boldsymbol{\xi}. \quad (3)$$

The first coefficients of the series, due to the definition of the Hermite polynomials, can be identified as the hydrodynamic moments (or a combination of those) of the distribution $f(\mathbf{x}, \boldsymbol{\xi}, t)$:

$$\mathbf{a}^{(0)} = \int f(\mathbf{x}, \boldsymbol{\xi}, t) \mathcal{H}^{(0)}(\boldsymbol{\xi}) d\boldsymbol{\xi} = \int f(\mathbf{x}, \boldsymbol{\xi}, t) d\boldsymbol{\xi} = \rho, \quad (4)$$

$$\mathbf{a}^{(1)} = \int f(\mathbf{x}, \boldsymbol{\xi}, t) \mathcal{H}^{(1)}(\boldsymbol{\xi}) d\boldsymbol{\xi} = \int f(\mathbf{x}, \boldsymbol{\xi}, t) \boldsymbol{\xi} d\boldsymbol{\xi} = \rho \mathbf{u} \quad (5)$$

and analogously for higher-order coefficients.

Due to the orthonormality of the Hermite polynomials,

$$f(\mathbf{x}, \boldsymbol{\xi}, t) \approx f^N(\mathbf{x}, \boldsymbol{\xi}, t) = \omega(\boldsymbol{\xi}) \sum_{n=0}^N \frac{1}{n!} \mathbf{a}^{(n)}(\mathbf{x}, t) \mathcal{H}^{(n)}(\boldsymbol{\xi}) \quad (6)$$

and $f^N(\mathbf{x}, \boldsymbol{\xi}, t)$ has the same leading N velocity moments as the complete $f(\mathbf{x}, \boldsymbol{\xi}, t)$.

It is possible now to describe the two mapping procedures:

- the DSMC2LB (or *projection*) step that allows to *project* the DSMC hydrodynamic variables (fine level of description) onto the LBM discrete distributions (coarse level of description);
- the LB2DSMC (or *reconstruction*) step that allows to *reconstruct* from the LBM discrete distributions (coarse level), the continuous, truncated, distribution function (fine level) from which the velocities of the DSMC particles can be sampled, e.g. via acceptance/rejection method.

It has to be noted that the following procedures can be extended to any suitable LB stencil whose discrete speeds are actually abscissae of a Gauss-Hermite quadrature.

2.1. DSMC2LB mapping scheme

Firstly, we present the DSMC2LB projection step. In correspondence with the DSMC cells/LBM nodes where the coupling occurs, the cumulative averages of the DSMC hydrodynamic variables, properly scaled (see Appendix A on how to perform such scaling), are used to compute the coefficients $\mathbf{a}_{\text{DSMC}}^{(n)}$ of the truncated distribution $f_{\text{DSMC}}^N(\mathbf{x}, \boldsymbol{\xi}, t)$ in Eq. (6).

We now take advantage of the fact that the distribution $f_{\text{DSMC}}^N(\mathbf{x}, \boldsymbol{\xi}, t)$ can be completely and uniquely determined by its values at a set of discrete velocities and, if the Gauss-Hermite quadrature is used, then the coefficients $\mathbf{a}_{\text{DSMC}}^{(n)}$ can be expressed as:

$$\begin{aligned} \mathbf{a}_{\text{DSMC}}^{(n)} &= \int f_{\text{DSMC}}^N(\mathbf{x}, \boldsymbol{\xi}, t) \mathcal{H}^{(n)}(\boldsymbol{\xi}) d\boldsymbol{\xi} = \\ &= \sum_{a=0}^{d-1} \frac{w_a}{\omega(\boldsymbol{\xi}_a)} f_{\text{DSMC}}^N(\mathbf{x}, \boldsymbol{\xi}_a, t) \mathcal{H}^{(n)}(\boldsymbol{\xi}_a), \end{aligned} \quad (7)$$

where w_a and $\boldsymbol{\xi}_a$ are the weights and abscissae of a Gauss-Hermite quadrature of algebraic precision of degree $\geq 2N$, and d is the total number of discrete

velocities of the quadrature.

The definitions of the first two hydrodynamic moments in the LBM are:

$$\rho = \sum_a f_a, \quad \rho \mathbf{u} = \sum_a f_a \boldsymbol{\xi}_a. \quad (8)$$

Comparing Eq. (7) with Eq. (8) and recalling the definitions of the Hermite polynomials $\mathcal{H}^{(n)}$ and that the coefficients $\mathbf{a}^{(n)}$ are the velocity moments of the $f^N(\mathbf{x}, \boldsymbol{\xi}, t)$, or a proper combination of those, it is immediate to see that the discrete distributions are the scaled values of the continuous distribution function evaluated at the Gauss-Hermite quadrature abscissae $\boldsymbol{\xi}_a$:

$$f_{\text{DSMC2LB},a}(\mathbf{x}, t) = \frac{w_a f_{\text{DSMC}}^N(\mathbf{x}, \boldsymbol{\xi}_a, t)}{\omega(\boldsymbol{\xi}_a)}. \quad (9)$$

105 Therefore, once the $f_{\text{DSMC}}^N(\mathbf{x}, \boldsymbol{\xi}, t)$ is built from the DSMC hydrodynamic moments and evaluated at the quadrature abscissae, $f_{\text{DSMC}}^N(\mathbf{x}, \boldsymbol{\xi}_a, t)$, the discrete (non-equilibrium) distributions to be supplemented to the LBM solver at the coupling nodes can be computed from Eq. (9).

2.2. LB2DSMC mapping scheme

The inverse reconstruction step (LB2DSMC) requires that at the LBM lattice nodes/DSMC cells where the coupling occurs, the velocities of the DSMC particles are sampled from a continuous distribution function.

At those lattice sites, the LBM discrete non-equilibrium functions $f_{\text{LB},a}$, are used to compute the coefficients of the expansion in Eq. (6):

$$\mathbf{a}_{\text{LB}}^{(n)} = \sum_{a=0}^{d-1} f_{\text{LB},a}(\mathbf{x}, t) \mathcal{H}^{(n)}(\boldsymbol{\xi}_a) \quad (10)$$

These allow to build the continuous truncated distribution $f_{\text{LB}}^N(\mathbf{x}, \boldsymbol{\xi}, t)$. To generate the velocities of the DSMC particles, the distribution should be sampled. Several algorithms can be employed to this aim. We chose to adopt an *acceptance/rejection* algorithm similar to the one presented in [22]. However, while in [22] a Chapman-Enskog distribution was sampled, in the present case a Grad's distribution has to be sampled but, nonetheless, most of the steps presented

there can be used here.

The Grad's velocity distribution, truncated up to order N , can be written as

$$g^N(\mathbf{x}, \boldsymbol{\xi}, t) = g^{(0)}(\boldsymbol{\xi})G(\mathbf{x}, \boldsymbol{\xi}, t) \quad (11)$$

where $g^{(0)}(\boldsymbol{\xi})$ is the weight function associated with the Hermite polynomials

$$g^{(0)}(\boldsymbol{\xi}) = \omega(\boldsymbol{\xi}) = \frac{1}{(2\pi)^{D/2}} \exp\left(-\frac{\boldsymbol{\xi}^2}{2}\right) \quad (12)$$

with D being the dimensionality of the flow problem. Eq. (12) represents also a global Maxwell-Boltzmann distribution at thermodynamic equilibrium (here we set a constant temperature $T = 1$ as we are interested in isothermal flows). At thermodynamic equilibrium $G(\mathbf{x}, \boldsymbol{\xi}, t) = 1$, while away from that condition, it can be expressed as:

$$G(\mathbf{x}, \boldsymbol{\xi}, t) = 1 + \frac{1}{2!} \mathbf{a}_{\text{LB}}^{(2)} \mathcal{H}^{(2)}(\boldsymbol{\xi}) + \frac{1}{3!} \mathbf{a}_{\text{LB}}^{(3)} \mathcal{H}^{(3)}(\boldsymbol{\xi}) + \dots + \frac{1}{N!} \mathbf{a}_{\text{LB}}^{(N)} \mathcal{H}^{(N)}(\boldsymbol{\xi}) \quad (13)$$

110 The steps followed in the generation of the velocities of DSMC particles are outlined in Table 1. Some comments on those steps. The acceptance/rejection method needs to define an envelope function $\gamma(\boldsymbol{\xi})$ such that $\gamma(\boldsymbol{\xi}) \geq g(\boldsymbol{\xi})$ for any $\boldsymbol{\xi}$. In step 3, an amplitude parameter C is set. In this way it is guaranteed that the function $\gamma(\boldsymbol{\xi}) = Cg^{(0)}(\boldsymbol{\xi})$ envelops most of the Grad's distribution function below it. The larger this parameter, the less probable is the chance that 115 $G(\mathbf{x}, \boldsymbol{\xi}, t)$ is larger than the envelop function, but at the same time, the smaller the efficiency of the sampling method since the efficiency is equal to $1/C$. In step 6, the particle velocity is generated as the sum of the thermal velocity and of the local fluid velocity. In Eq. (17), the thermal velocity is determined according to the temperature value and to the molecular mass of the gas as set in 120 the DSMC simulation.

Apart from the velocity, also the number of the DSMC particles, N_{LB2DSMC} , must be set in order to guarantee conservation of mass at the coupling sites so that the density from LBM and the density from DSMC, appropriately scaled, 125 match with each other.

**Sampling acceptance/rejection algorithm
for the Grad's distribution LB2DSMC**

1. Compute the coefficients

$$a_{\text{LB},ij}^{(2)} = \sum_a f_{\text{LB},a}(\xi_{a,i}\xi_{a,j} - \delta_{ij}) \quad (14)$$

and similarly for the higher-order ones

2. Find

$$M \equiv \max \left(\left| a_{\text{LB},ij}^{(2)} \right|, \left| a_{\text{LB},ijk}^{(3)} \right|, \dots, \left| a_{\text{LB},ijk\dots}^{(N)} \right| \right) \quad (15)$$

3. Set the parameter

$$C = 1 + 30M \quad (16)$$

4. Sample a try particle velocity $\boldsymbol{\xi}_{\text{try}}$ from the Maxwell-Boltzmann distribution $g^{(0)}(\boldsymbol{\xi})$ using e.g. the Box-Müller transformation method

5. Accept the $\boldsymbol{\xi}_{\text{try}}$ if $C\mathcal{R} \leq G(\mathbf{x}, \boldsymbol{\xi}_{\text{try}}, t)$ with \mathcal{R} a uniform deviate in the interval $[0, 1)$ otherwise reject it and go back to step 4

6. Generate the DSMC particle velocity as

$$\mathbf{v}_{j,\text{LB2DSMC}} = \left(\frac{2k_B T_{\text{DSMC}}}{m_{\text{DSMC}}} \right)^{1/2} \boldsymbol{\xi}_{\text{try}} + \mathbf{u}_{\text{LB}} \quad (17)$$

Table 1: Steps of the sampling acceptance/rejection algorithm for the LB2DSMC reconstruction mapping scheme used to generate the velocities of DSMC particles from LBM data.

In Figure 1, the schematic showing the main steps involved in both the mapping schemes is drawn.

It is interesting to try to identify sources of inaccuracy in the proposed mapping scheme. In the reconstruction and projection steps, in fact, some information

130 is inevitably lost. In particular, in the LB2DSMC reconstruction step, the truncated distribution, $f_{\text{LB}}^N(\mathbf{x}, \boldsymbol{\xi}, t)$, is derived from the discrete distributions, $f_{\text{LB},a}(\mathbf{x}, t)$. This truncated distribution is such that only the first N moments are the same as those of the non-truncated continuous distribution $f(\mathbf{x}, \boldsymbol{\xi}, t)$, with the value of N essentially depending on the particular quadrature used.

135 The moments of order higher than N , in fact, will not be the same as those of the original continuous distribution. This, in turn, reflects in the fact that the DSMC particles will be given a velocity which is sampled from a distribution which accurately recovers up to the first N moments. If, then, the sampling process were perfectly able to sample the velocity distribution $f_{\text{LB}}^N(\mathbf{x}, \boldsymbol{\xi}, t)$, then

140 also the moments computed from the velocities of the particles would be perfectly reproduced in the limit of an infinite number of independent samples. However, since only a finite number of samples can be obtained, measurements of moments will be affected by statistical noise which will be also present in the discrete distribution functions $f_{\text{DSMC2LB},a}(\mathbf{x}, t)$.

145 Analogously, in the DSMC2LB projection step, the loss of information derives from the fact that only the first N moments are used to evaluate the truncated discrete distributions $f_{\text{DSMC2LB},a}(\mathbf{x}, t)$, while, in principle, the DSMC solution possesses information on all the moments up to $N \rightarrow \infty$. The truncation, again, is performed according to the algebraic degree of accuracy of the particular LB

150 quadrature. To be more precise, this does not imply that moments of order larger than N cannot be evaluated but it means that they are not accurately computed. If the so found discrete distributions were used to build a continuous distribution from which to sample the velocities of the DSMC particles, then the source of inaccuracy would be mainly related to the acceptance/rejection

155 algorithm and in particular on the choice of parameter C in Eq. (16) which determines the extension of the envelope function $\gamma(\boldsymbol{\xi})$.

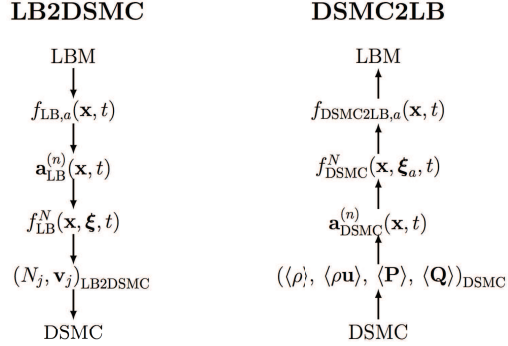


Figure 1: Schematic showing the main steps of the top-down LB2DSMC reconstruction (left) and bottom-up DSMC2LB projection (right) mapping schemes as described in Section 2. \mathbf{P} and \mathbf{Q} represent the second and third order momentum flux tensors, respectively. Symbol $\langle \rangle$ represents the cumulative average measurements of hydrodynamic moments from the DSMC solver.

3. Numerical results

3.1. Comparison between DSMC and LBM data

To understand and determine the extent of the overlap region where both DSMC and LBM provide comparable accuracy in simulating rarefied gas flows, we performed independent force-driven plane Poiseuille flow simulations with two parallel plates at $x = 0$ and $x = H$ and compared results obtained from D3Q19 and D3Q39 LB models with DSMC data. Even if the flow is strictly a monodimensional flow, we used 3D solvers since our final aim is to be able to simulate more complex flows. This choice reflects in the fact that double periodic boundary conditions are imposed along the y - and z - directions. Tests are performed at different Kn number, based on channel height, while keeping constant the Ma number, based on the flow centerline velocity, u_{max} : $\text{Ma} = u_{max}/c_s = 0.1$. The Ma number is set to such a value to guarantee that the lattice equilibria in LBM, expressed as a second-order (D3Q19) or a third-order (D3Q39) expansion in Ma number of the local Maxwellian, are positive defined, but it is still sufficiently high to prevent DSMC simulations from becoming impractically computationally expensive.

In the BGK-LBM simulations, we set the flow Kn number imposing the relaxation time τ according to the relation [46, 47]:

$$\tau = \sqrt{\frac{\pi}{8}} \frac{c}{c_s} \text{KnH} + 0.5 \quad (18)$$

where c/c_s is equal to $\sqrt{3}$ for the D3Q19 model and to $\sqrt{3/2}$ for the D3Q39 model, and H is the number of lattice sites along the channel height. Once Kn and H are set, τ is also set. For both D3Q19 and D3Q39 models, kinetic boundary conditions and regularization procedure are applied.

In the DSMC simulations, we set the Kn number imposing the height of the channel, H, and the mean free path λ . To set λ , a proper number density n and a collision model should be defined. In the case of Hard Sphere (HS) model, the relation between λ and n (at equilibrium) is given by [6]:

$$\lambda = \frac{1}{\sqrt{2}\pi d_{\text{ref}}^2 n} \quad (19)$$

where d_{ref} is a reference molecular diameter. The determination of λ from Eq. (19) and estimates on the molecular speed allows to define the space and time discretizations.

Once the number of cells along the channel height is determined from DSMC parameters, an equal number of lattice sites is imposed in the LBM simulation so that the cells centers in DSMC and the LBM lattice sites overlap.

In Figure 2, the velocity profiles along the direction of the forcing, obtained from the LB models and DSMC, normalized with the centerline velocity, are shown for Kn=0.15.

In the DSMC an *Argon*-like gas has been simulated and the grid resolution, kept the same for all performed tests, is based on the requirements of a DSMC simulation at Kn=0.05. In all the DSMC simulations, 100 computational molecules are initially placed in each cell of the domain.

LB solution has been considered as converged to the final solution once the following criterion is fulfilled:

$$\sum_i \frac{|\mathbf{u}(\mathbf{x}_i, t) - \mathbf{u}(\mathbf{x}_i, t-1)|}{|\mathbf{u}(\mathbf{x}_i, t)|} < 10^{-6}. \quad (20)$$

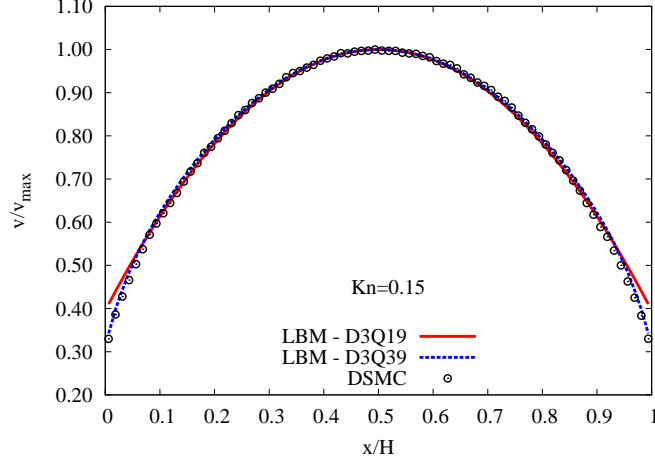


Figure 2: The velocity profiles of the planar force-driven Poiseuille flow for $\text{Kn}=0.15$. The LBM results with both the D3Q19 and D3Q39 models are compared with the DSMC solution. For both the LB models the regularization procedure is applied. Fully diffuse reflection is imposed at the walls, $x/H = 0$ and $x/H = 1$, for both the LBM and DSMC simulations.

In Eq. (20), $\mathbf{u}(\mathbf{x}_i, t)$ represents the fluid velocity at the lattice nodes at time t . For DSMC, instead, a 1% fractional error on fluid velocity components is set as the requirement to assume the solution as converged; see Section 5 for the implications in the number of required time steps to achieve such error.

Plots similar to the one of Figure 2, have been drawn also for other Kn numbers but they are not reported here. It is more informative, in fact, to inspect the relative errors between DSMC and LBM data as done in Figure 3. The relative error is defined as:

$$\Delta v = \frac{v_{LBM} - v_{DSMC}}{v_{LBM}} \quad (21)$$

and it is shown for simulations at $\text{Kn}=0.10-0.25$.

In the plots of Figure 3, moreover, the boundaries of the Knudsen layer (black dashed vertical lines) are also drawn. The Knudsen layer is a region in proximity of a solid wall which extends within the flow domain up to a distance of the order of one mean free path. Inside this region non-equilibrium effects of the flow are stronger [48, 49]. It is also within this layer that departures between

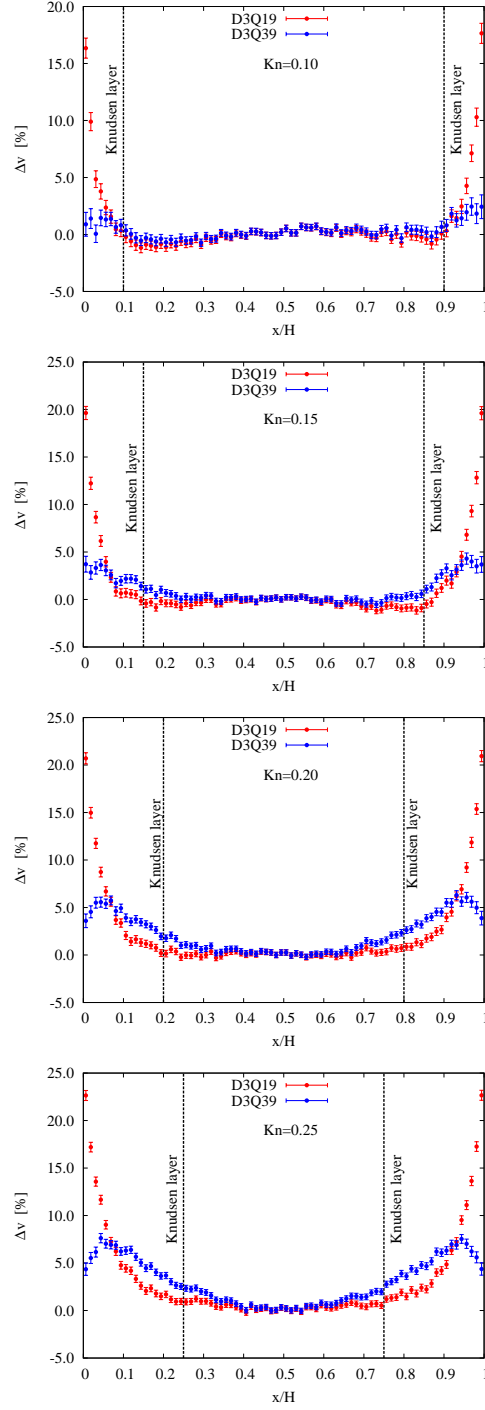


Figure 3: Relative error between LBM results and DSMC data, according to Eq. (21) for $Kn=0.10 - 0.25$. Dashed vertical lines represent the boundaries of the Knudsen layer. Error bars from DSMC simulations on fluid velocity are shown.

the numerical methods become apparent. In fact, while both LB models provide comparable results in the bulk of the flow, within the Knudsen layer they differ significantly. The D3Q19 lattice, in fact, recovering up to the Navier-Stokes level of description only, is rather inaccurate in this part of the domain. The
175 D3Q39 lattice, instead, is able to reproduce the DSMC data to a much better degree of accuracy. However, already at $Kn=0.25$, it is possible to notice some deviations also within the Knudsen layer as the maximum relative error is about equal to 7.5%. This behavior can be explained taking into account that non-equilibrium effects at an order higher than the third may start to play a role.
180 With this statement, we do not imply that LBM is able to reliably simulate rarefied gas flows only for $Kn \leq 0.25$, but that with the current LB model we found reasonable agreement with DSMC data up to that Kn number. With larger Gauss-Hermite quadratures, in fact, being able to go beyond the third-order in Hermite polynomials expansion guaranteed by the D3Q39, further non-
185 equilibrium effects should be correctly captured. However, we decided not to go further because the next quadrature possessing a high enough algebraic precision to allow an accurate fourth-order in Hermite polynomials expansion involves 91 discrete speeds [50].

3.2. Numerical results for the DSMC2LB mapping scheme

190 Having concluded that the LBM D3Q39 model provides, for the problem at hand, a reasonable accurate solution for $Kn \leq 0.25$, we analyze results related to the mapping scheme step that allows to project the DSMC hydrodynamic variables onto the LBM discrete distribution functions for the D3Q39 lattice (DSMC2LB projection step).

195 To be noted that the unit conversion as delineated in Appendix A to pass from SI units, proper of the DSMC method, to the lattice units, proper of the LB method, is applied during simulations. To validate the procedure outlined in Section 2.1, we ran two sets of independent DSMC and LBM simulations under the same force-driven plane Poiseuille flow with Ma based on the centerline
200 velocity equal to 0.1 and for several Kn numbers. We verified the accordance

between the discrete distributions functions as computed from the LBM, $f_{\text{LB},a}$, and as obtained from the DSMC2LB projection scheme, $f_{\text{DSMC2LB},a}$, applying Eq. (9). In Figure 4, a sketch showing the procedure to compare the $f_{\text{LB},a}$ with the $f_{\text{DSMC2LB},a}$ is depicted. Data refers to the first fluid node/cell in proximity to the wall located at $x = H$ as shown in the sketch of Figure 5. In Figure 6 the ratio $f_{\text{DSMC2LB},a}/f_{\text{LB},a}$ is plotted for all discrete speeds $a = 0, \dots, d-1$ and for $\text{Kn}=0.15$ and $\text{Kn}=0.25$. The larger errors that can be detected are about equal to 2% ($f_{\text{DSMC2LB},36}/f_{\text{LB},36} \approx 1.02$) and to 5% ($f_{\text{DSMC2LB},36}/f_{\text{LB},36} \approx 1.05$) for the simulations at $\text{Kn}=0.15$ and 0.25 , respectively. Most of the other ratios are such that the error is below 1%.

The error bars present in the plots derive from the fact that we use the DSMC hydrodynamic moments to build the truncated distributions $f_{\text{DSMC}}^N(\mathbf{x}, \boldsymbol{\xi}_a, t)$ and those are inherently characterized by statistical noise.

We also note that the larger error bars are present for the discrete speeds with larger module. This may be attributed to the fact that the magnitude of the discrete distribution function, f_a , is smaller the larger the module of the corresponding discrete speed, $\boldsymbol{\xi}_a$, while the statistical noise does not depend on the particular discrete speed.

From the comparison of the discrete distributions, f_a , only, however, it is difficult to understand if the projection mapping scheme is providing accurate results. So it is more informative to compute the hydrodynamic moments from $f_{\text{LB},a}$ and from $f_{\text{DSMC2LB},a}$ at the same node depicted in Figure 5. The first few moments are reported in Table 2.

It can be seen that a good matching is found always within the error bars.

Concluding, the projection mapping scheme is able to pass from the DSMC hydrodynamic quantities to the LBM discrete distributions preserving a reasonable level of accuracy.

3.3. Numerical results for the LB2DSMC mapping scheme

We now move on to analyse the results related to the reconstruction mapping scheme step that allows to reconstruct from the LBM discrete distributions,

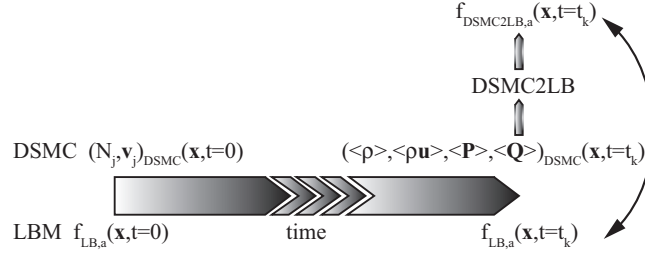


Figure 4: Schematic representing the procedure used to compare the discrete populations built from the DSMC hydrodynamic moments following the projection DSMC2LB algorithm, $f_{DSMC2LB,a}(\mathbf{x}, t = t_k)$, with native discrete populations obtained from an independent LBM simulation, $f_{LB,a}(\mathbf{x}, t = t_k)$, under the same flow conditions, namely Kn and Ma, at time $t = t_k$, when the steady-state condition is reached.

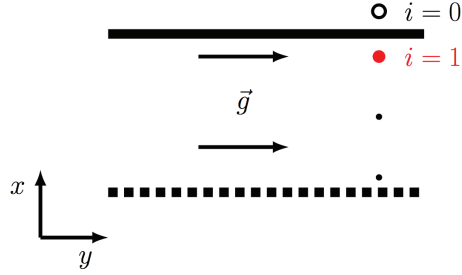


Figure 5: Sketch showing the location of the node (red node at $i = 1$) where data plotted in Figures 6, and 8 are taken. \vec{g} represents the body force driving the fluid.

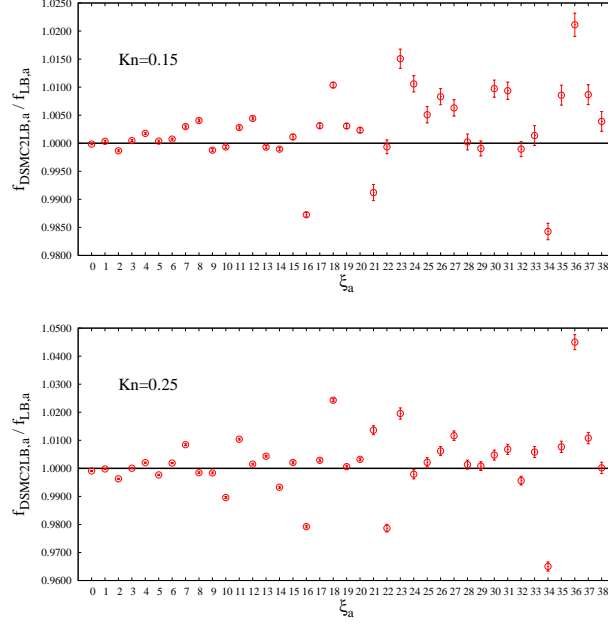


Figure 6: Ratio $f_{\text{DSMC2LB},a}/f_{\text{LB},a}$ where $f_{\text{DSMC2LB},a}$ are computed from Eq. (9) for plane Poiseuille flow at $\text{Kn}=0.15$ (top) and at $\text{Kn}=0.25$ (bottom).

Kn=0.15	ρ [l.u.]	ρu_y [l.u.]	$P_{xy} + \rho u_x u_y$ [l.u.]
LBM	1.0	0.0282	-0.0151
DSMC2LB	1.002 ± 0.007	0.0277 ± 0.0042	-0.0146 ± 0.0027
Kn=0.25	ρ [l.u.]	ρu_y [l.u.]	$P_{xy} + \rho u_x u_y$ [l.u.]
LBM	1.0	0.0352	-0.0180
DSMC2LB	0.999 ± 0.007	0.0340 ± 0.0042	-0.0167 ± 0.0024

Table 2: Comparison between the first few moments as computed from $f_{\text{DSMC2LB},a}$ obtained from the projection mapping scheme and from the native LBM simulations, $f_{\text{LB},a}$, at the node depicted in Figure 5. Moments are expressed in lattice units.

$f_{\text{LB},a}$, the continuous truncated distribution function from which the velocities of the DSMC particles can be sampled (LB2DSMC reconstruction step).

The unit conversion as delineated in Appendix A to pass from lattice units, proper of the LB method, to the SI units, proper of the DSMC method, is

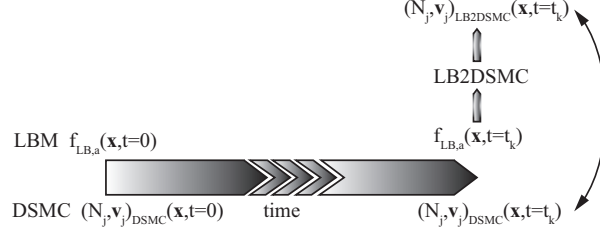


Figure 7: Schematic representing the procedure used to compare the distribution function of the velocity component, $v_{j,DSMC}$, obtained from a native DSMC simulation with the distribution function of the velocity of the particles, $v_{j,LB2DSMC}$, obtained from the reconstruction mapping algorithm LB2DSMC, under the same flow conditions, namely Kn and Ma , at time $t = t_k$, when the steady-state condition is reached.

235 applied during simulations. As done for the previous step, to validate the procedure outlined in Section 2.2, we ran two independent set of DSMC and LBM simulations under the same force-driven plane Poiseuille flow with $Ma=0.1$ and for several Kn numbers.

As shown in Figure 7, we compared the velocity distribution functions as obtained from the DSMC simulation collecting the velocities, $\mathbf{v}_{j,DSMC}$, of the particles residing at the cell identified in Figure 5 and as obtained from the velocities of the particles sampled from the velocity distribution function built as in Eq. (11) using the algorithm outlined in Table 1, $\mathbf{v}_{j,LB2DSMC}$.

In Figure 8, in particular, the distributions for the velocity component along the direction of the forcing, v_y , are compared for $Kn=0.15$ and $Kn=0.25$, respectively.

The mean and the standard deviation for the two cases are collected in Table 3.

The velocities of the particles are collected for both cases after a steady-state condition has been reached. The deviations between the means, about 4% for the case at $Kn=0.15$ and about 5% for the case at $Kn=0.25$, are in line with the deviations that are present in Figure 3. The standard deviations of the two distributions differ for about 0.3% for both the cases. Related to this, it has to be recalled that the temperature of Eq. (17) is the reference temperature im-

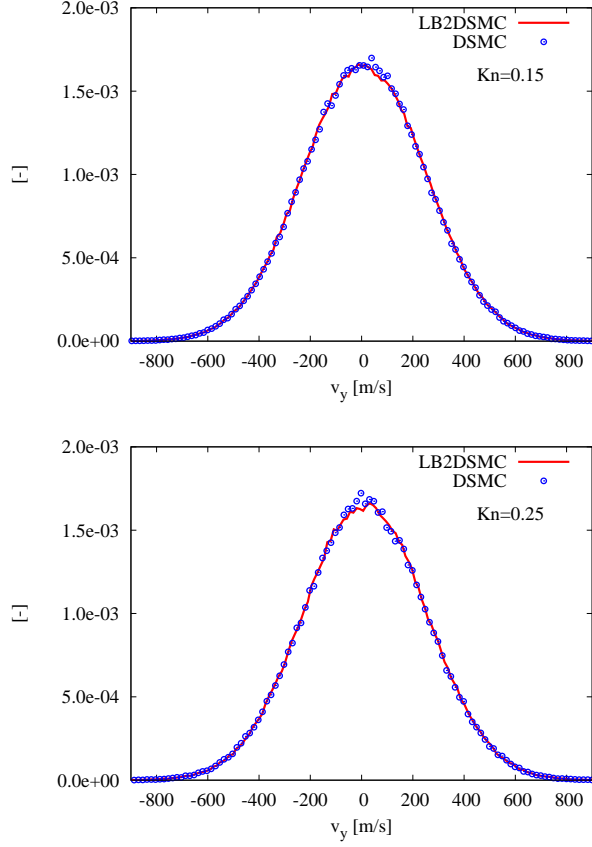


Figure 8: Distribution functions for the y-component, v_y , of the velocity of the particles, expressed in DSMC units, as obtained from the native DSMC simulation and from the reconstruction mapping scheme using the algorithm LB2DSMC outlined in Table 1 for $Kn=0.15$ (top) and $Kn=0.25$ (bottom), for the cell identified in Figure 5.

Kn=0.15	$\langle v_y \rangle$ m/s	σ_{v_y} m/s
DSMC	10.1	238.6
LB2DSMC	10.5	239.3
Kn=0.25	$\langle v_y \rangle$ m/s	σ_{v_y} m/s
DSMC	12.8	238.8
LB2DSMC	13.4	239.6

Table 3: Comparison of the means and standard deviations of the distributions of Figures 8, expressed in DSMC units.

posed in the DSMC simulation. The magnitudes of these standard deviations
255 are compatible with the reference temperature ($T=273$ K) and the molecular
mass ($m = 6.63 \cdot 10^{-26}$ kg) for the gas used in the DSMC simulation.

It is important, however, that also the distributions of the realizations of the
fluid velocity as obtained from DSMC and from the reconstruction mapping
scheme match with each other. This is checked computing the fluid velocities as
260 the instantaneous average velocity from all the velocities of particles residing in
the chosen cell at regular time intervals (samples are taken once every 50 time
steps) so to have uncorrelated samples. Also in this case, data are collected
once the flow has reached a steady-state condition.

In Figure 9, the fluid velocity distributions are plotted for the case $Kn=0.15$.
265 Both the mean and standard deviations of the distributions obtained from the
two methods are in good agreement, demonstrating that the LB2DSMC recon-
struction step correctly maps the discrete LB distribution functions into the
velocities of the DSMC particles.

4. Hybrid model application

As a *proof of concept* of a prospective LB-DSMC coupling, we applied a
hybrid model to a plane Poiseuille flow with $Kn=0.05$ and $Ma=0.1$, based on
centerline velocity.

In Figure 10, the geometry for the application of the hybrid method is drawn.

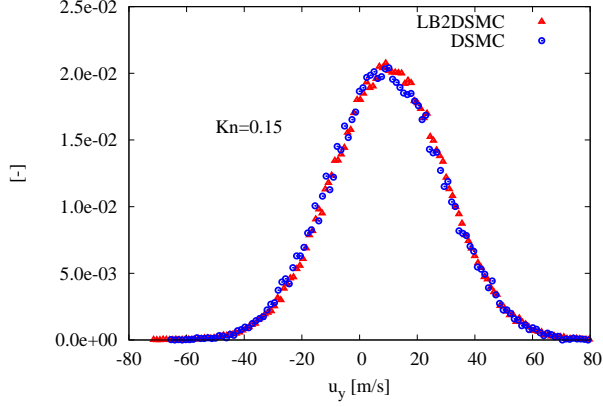


Figure 9: Fluid velocity distribution functions for the y-component, u_y , expressed in DSMC units, as obtained from the native DSMC simulation and from the reconstruction mapping scheme using the algorithm LB2DSMC outlined in Table 1 for $Kn=0.15$, for the cell identified in Figure 5.

The domain is divided into two subdomains. In each subdomain, one solution method is applied. In particular, we assume that, at a section located at $y = L_0/2$, the two subdomains overlap and this *buffer layer* is composed by one cell along the flow direction and extends across the whole height H of the channel.

For simplicity, since we wanted to set up the functionality of the coupling, we use a D3Q19 LB model with kinetic boundary conditions and no regularization. The mapping scheme, also, is simpler than the one proposed in Section 2. In particular, we imposed that, at the centers of DSMC cells/LBM lattice sites within the buffer layer, the local equilibria are evaluated according to the hydrodynamic moments computed from the DSMC solution.

Operatively, we set the discrete equilibrium distribution functions, $f_{\text{DSMC2LB},a}^{(0)}$, within the buffer layer as:

$$f_{\text{DSMC2LB},a}^{(0)} = w_a \rho_{\text{DSMC}} \left[1 + \frac{\boldsymbol{\xi}_a \cdot \mathbf{u}_{\text{DSMC}}}{c_s^2} + \frac{(\boldsymbol{\xi}_a \cdot \mathbf{u}_{\text{DSMC}})^2}{2c_s^4} - \frac{u_{\text{DSMC}}^2}{2c_s^2} \right] \quad (22)$$

270 In Figure 11, we plot the evolution in time of the velocity profiles obtained from the hybrid method for the test previously introduced.

The three plotted profiles represent the data at the three sections along the channel located at $y = L_0/4$, $y = L_0/2$ and $y = 3L_0/4$. The section at $y = L_0/4$ is within the DSMC subdomain, while the section at $y = L_0/2$ coincides with the
275 buffer layer position and the section at $y = 3L_0/4$ is within the LBM subdomain. From the plots of Figure 11, it is possible to see that the inherent statistical noise of the DSMC solution is *transferred* to the LBM velocity profiles. While averaging over time, this noise is reduced and also the LBM solution becomes accordingly, smoothened. Note that, in the DSMC solver, no particular means
280 to reduce statistical noise, such as variance-reduction methods, [51–53], has been adopted. Thus, there is certainly room for significant future improvements.

From inspection of Figure 11, it is possible to detect deviations between the DSMC velocity profile ($y = L_0/4$) and the LBM velocity profile ($y = 3L_0/4$) when the steady state is reached (see the plot at $t = 1600$). These deviations
285 can be attributed to the limitations of both the LB model and mapping scheme adopted in this test, as all the non-equilibrium effects have been discarded.

The deviations will be removed by adopting the LB model able to extend the range of applicability of the LBM to rarefied gas flows and by including non-equilibrium effects in the passage of information between the DSMC and the
290 LBM as described in Section 2. This fully non-equilibrium hybrid model is under development.

5. Computational efficiency

We conclude by comparing the computational efficiency of the two methods and by estimating the computation times of the hybrid method with respect to a full DSMC simulation.

Both the DSMC and LBM codes are parallelized. All data presented in this section are from simulations run on a dual-core PC (Intel Core i5-6300U 2.4 GHz) with hyperthreading enabled and refer to the test cases of Sections 3.1

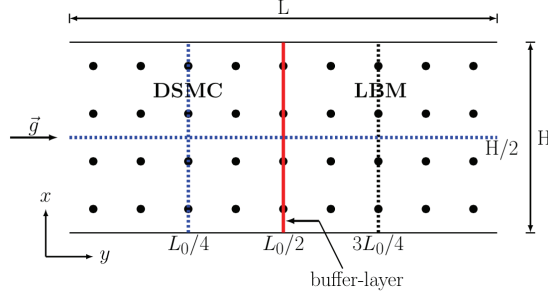


Figure 10: Schematic picture of the hybrid model application domain. The coupling occurs at the LBM lattice sites/DSMC cells placed at $y = L_0/2$. The buffer layer comprises only one cell in the streamwise direction and all the cells along the transversal direction. The positions $y = L_0/4$ and $y = 3L_0/4$ identify the streamwise positions where the velocity profiles plotted in Figure 11 are evaluated.

and 4.

In Figure 12, the wall-clock time per computational time step is plotted as a function of the flow Kn number for both LBM models (D3Q19 and D3Q39 with the regularization procedure and kinetic boundary conditions) and DSMC. The wall-clock time per time step is constant for the LBM simulations while it shows a dependence on Kn for the DSMC method.

This might be explained considering that in DSMC, as kinetic theory prescribes, the total number of interparticle collisions scales with the number density. For the NoTimeCounter (NTC) algorithm, [6], as the one employed here, one has:

$$N_{\text{collis}}(t_k, x_j) = \frac{1}{2} N \bar{N} F_N (\sigma_T c_r)_{\text{max}} \Delta t / V_c \quad (23)$$

where $N = n(t_k, x_j) V_c / F_N$, with n number density at time t_k and cell j , V_c the cell volume and F_N the number of real molecules represented by a simulated computational particle, $\bar{N} = \langle N \rangle$, σ_T the molecular cross section, c_r the relative velocity between the selected particles to undergo collision, Δt is the time step duration. In Eq. (23), the term $(\sigma_T c_r)_{\text{max}}$ is the maximum value of the product between the collision cross section and the relative velocity between the selected particles in each grid cell.

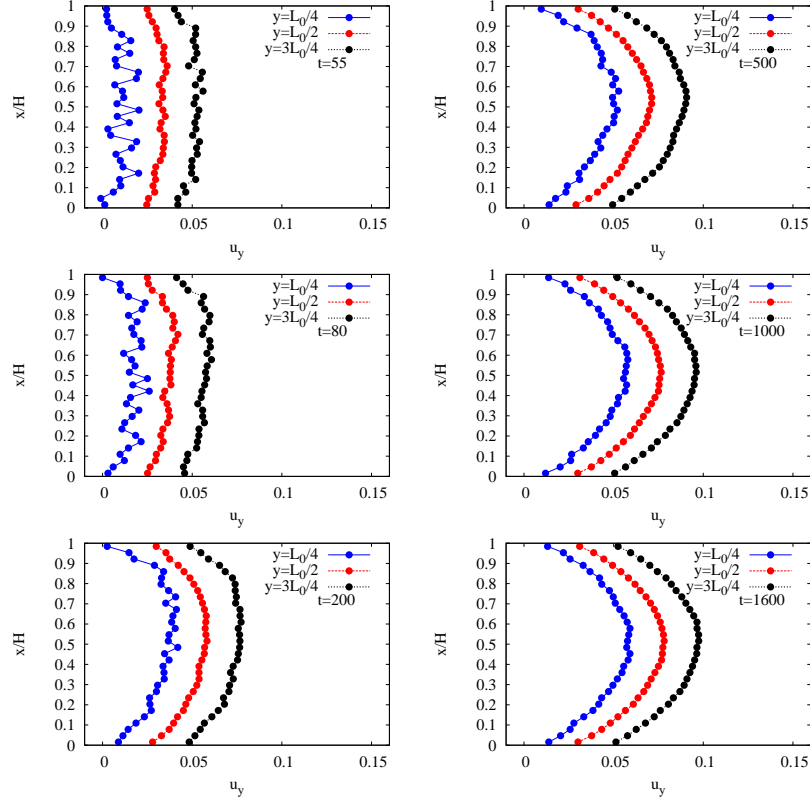


Figure 11: Evolution in time of the flow when the simplified mapping scheme DSMC2LB is activated at $y = L_0/2$. Velocity profiles are plotted in correspondence of the channel sections identified in Figure 10. The velocity profiles, expressed in lattice units, at $y = L_0/2$ and $y = 3L_0/4$ are shifted $+0.02$ and $+0.04$, respectively, to allow better visualization.

From Eq. (23) the larger the Kn number, the smaller the number density n and the smaller the total number of collisions. However, since the same number of cells and particles are used for all the simulations and since the collision step in the DSMC method is just one part of the algorithm, only a small decrease in the wall-clock time of the single computational time step is achieved while increasing Kn number. In the LBM, instead, Kn number determines the relaxation time τ but different values of τ do not affect the computational efficiency of the single computational step.

From Figure 12, it is also evident the fact that LBM wall-clock times are smaller than the ones for DSMC. In particular, a single computational time step for the D3Q19 model is 5 times faster and for the D3Q39 model is 2 times faster than for the DSMC.

These numbers, however, do not tell the full story because DSMC is intrinsically characterized by statistical noise due to thermal fluctuations. This greatly affects the computational efficiency of the DSMC in comparison with LBM.

In fact, to reduce the statistical noise on DSMC hydrodynamic moments, time (or ensemble) averaging is needed. For example, one standard deviation on the fluid velocity components measurement, σ_{u_i} , is given (at equilibrium) by [54]:

$$\sigma_{u_i} = \sqrt{\frac{k_B \langle T \rangle}{m \langle N \rangle}} \frac{1}{\sqrt{S}} \quad (24)$$

where $\langle T \rangle$ and $\langle N \rangle$ are the averages of temperature and number of computational particles in a cell and S is the number of independent statistical samples. An estimate on the statistical error on the evaluation of the fluid velocity is given as:

$$\begin{aligned} E_{u_i} = \frac{\sigma_{u_i}}{|\langle u_i \rangle|} &= \sqrt{\frac{k_B \langle T \rangle}{m \langle N \rangle}} \frac{1}{\sqrt{S}} \frac{1}{|\langle u_i \rangle|} \\ &= \frac{1}{\sqrt{\gamma \langle N \rangle S} \text{Ma}} \end{aligned} \quad (25)$$

where γ is the gas specific heat ratio (1.67 for *Argon*) and Ma is the Mach number.

If a 1% fractional error is desired, for a $\text{Ma}=0.1$ flow and $\langle N \rangle = 100$, $S \approx 3600$

independent samples are needed. Generally, to obtain independent samples 10-100 time steps between the samples are required. In all the simulations in this work, we decided to perform the sampling every 50 time steps. Calculation of the correlation coefficients between sampled quantities showed that, for the flow of these tests, a 50 time steps interval is sufficient, e.g.:

$$\text{corr}(u_x, u_y) = \frac{\langle \delta u_x \delta u_y \rangle}{\sqrt{\langle \delta u_x^2 \rangle \langle \delta u_y^2 \rangle}} = -0.008. \quad (26)$$

Estimates on the number of needed independent samples to reach a given fractional error and on the size of the time steps interval so to obtain independent samples allow to determine the number of the required total computational time

295

steps. So, for the tests we performed, at least 180000 time steps are needed. For the LBM, instead, a steady-state solution is reached in few thousands time steps. About 5000 time steps are sufficient to reach the final solution.

These numbers directly reflect in the comparison between the total wall-clock times needed for the DSMC and LBM simulations. Using data collected in Figure 12, if the DSMC is compared with the D3Q19 model, then the latter is about 180 times faster, while if the comparison is made with the D3Q39 model, then the latter is about 70 times faster. Moreover, a reduction in the total number of DSMC particles guaranteed by reducing the domain assigned to the DSMC reflects in a reduction in the wall-clock time per time step as shown in Figure 13 where a linear scaling is found for the range of particles typically employed for the flow under consideration.

300

305

Finally, these numbers allow to estimate the potential gain in efficiency that can be obtained by the application of the hybrid model.

Using the simplified mapping scheme to pass from DSMC to LBM as described in Section 4 and assuming that the domain is divided into two subdomains of equal size, then a speed-up of about 1.7 with respect to a full DSMC simulation over the whole domain is reachable for the tested Poiseuille flow. To be noted that the over-head due to the application of the simplified mapping scheme is very limited since the buffer layer is composed of just one layer of cells/lattice nodes. For more complicated flows, however, coupling may be required to be

310

315

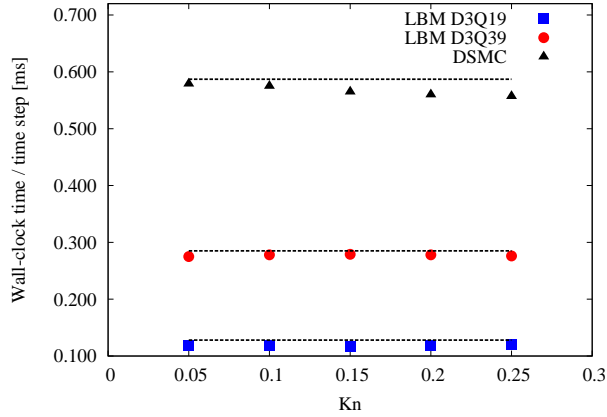


Figure 12: Wall-clock time per computational time step in LBM D3Q19, LBM D3Q39 and DSMC for the test of Section 3.1. While LBM data wall clock time does not depend on Kn number, DSMC data show a mild dependence on Kn. Note that both LBM and DSMC simulations, as stated in Section 3.1, are run on a grid based on the requirements for the DSMC simulation at Kn=0.05 and kept the same for all the simulations at different Kn number. 32000 particles are employed for the DSMC simulations.

applied over larger overlapping zones.

6. Conclusions

We developed a kinetic mapping scheme based on Grad's moments method
 320 and Gauss-Hermite quadrature in view of coupling DSMC and LBM models to
 simulate isothermal flows with non-uniform rarefaction effects. The main steps
 of the mapping algorithm between DSMC and LBM in order to allow an accu-
 rate passage between the two methods domains were discussed. To extend the
 range of applicability of LBM beyond the Navier-Stokes equation level, and thus
 325 postponing the passage to the DSMC solver, the need for adopting a high-order
 lattice (D3Q39) and a regularization procedure for the LBM is demonstrated by
 finding a good agreement between the DSMC and LBM velocity profile for plane
 Poiseuille flow up to Kn=0.25. As a proof of concept of the hybrid method, a
 simpler version of the mapping scheme which enforces the passage through local

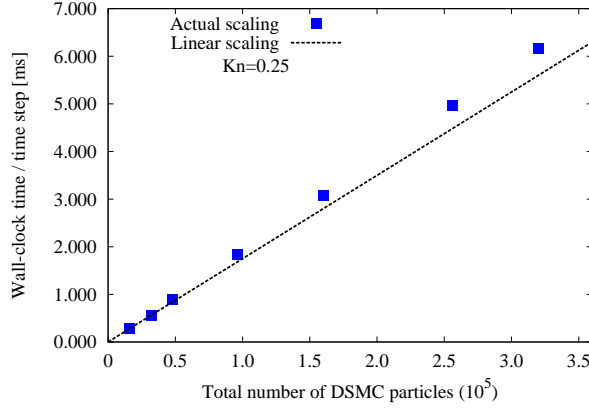


Figure 13: Wall-clock time per time step for DSMC as a function of the total number of particles for a simulation at $Kn=0.25$. Linear scaling is shown for the range of particles per cell typically employed in DSMC simulations. Savings in the total number of particles reflect in a linear reduction of the total wall-clock time of the simulation. The simulated flow is the same presented in Section 3.1.

330 equilibrium states has been performed for the simulation of a plane Poiseuille flow at $Kn=0.05$. We have also estimated that the adoption of the hybrid scheme significantly increases computational efficiency with respect to a DSMC simulation performed over the whole domain by a factor equal to 1.7 for the flow conditions shown in the test case. The adoption within the hybrid model of the
 335 complete mapping scheme including non-equilibrium effects is currently under development.

Acknowledgements

This research is supported by the Dutch Technology Foundation STW, which is part of the Netherlands Organisation for Scientific Research (NWO), and
 340 which is partly funded by the Ministry of Economic Affairs.

Appendix A. Scaling factors

To be able to apply the proposed methods also in engineering contexts and in parallel with experiments, we decided to employ in the DSMC simulations dimensional variables with SI units. This implies that, prior to any transfer of
 345 information between LB and DSMC, a proper conversion from lattice units to SI units, or vice versa according to the fact that the DSMC2LB or LB2DSMC mapping scheme is involved, has to be performed.

The basic elementary conversion scales are here introduced:

- *Length scale*

Since in LB we assume the lattice spacing Δx as the space unit and since we impose that the centers of the DSMC cells overlap with the LB sites, then the length scale is set as:

$$L_0 = \Delta x_{\text{DSMC}} \quad [\text{m}], \quad (\text{A.1})$$

where Δx_{DSMC} is the linear distance between the centers of two adjacent
 350 DSMC cells. Note that this implies that, at least in the buffer layer, the DSMC cells are cubic;

- *Time scale*

Similarly, the time unit within the LB simulation is the elementary lattice time-step. The physical value can be defined through the speed of sound within the lattice, c_s , and of the gas in the DSMC simulation, a , as

$$T_0 = \frac{c_s}{a} \Delta x_{\text{DSMC}} \quad [\text{s}]. \quad (\text{A.2})$$

- *Mass scale*

As the mass within the DSMC cells/LB nodes where coupling occurs must be conserved, and assuming the lattice particles are given a unit mass, then the mass scale can be defined as follows:

$$M_0 = \frac{F_{N,\text{DSMC}} N_{\text{DSMC}} m}{\sum_a f_{\text{LB},a}} \quad [\text{kg}], \quad (\text{A.3})$$

where $F_{N,\text{DSMC}}$ is the number of real molecules represented by one DSMC particle, N_{DSMC} is the number of DSMC particles in a cell, and m is the gas molecular mass.

355 From these three scaling factors, it is possible to derive all the other physical conversion scales.

References

References

- [1] C.-M. Ho and Y.-C. Tai, “Micro-electro-mechanical-systems (mems) and fluid flows,” *Annu. Rev. Fluid Mech.*, vol. 30, pp. 579–612, 1998.
- 360 [2] J. M. Reese, M. A. Gallis, and D. A. Lockerby, “New directions in fluid dynamics: non-equilibrium aerodynamic and microsystem flows,” *Phil. Trans. R. Soc. Lond. A*, vol. 361, pp. 2967–2988, 2003.
- [3] G. Karniadakis, A. Beskok, and N. Aluru, *Microflows and Nanoflows. Fundamentals and Simulation*. New York: Springer-Verlag, 2005.
- 365 [4] I. D. Boyd, G. Chen, and G. V. Candler, “Predicting failure of the continuum fluid equations in transitional hypersonic flows,” *Phys. Fluids*, vol. 7, p. 210, 1995.
- [5] K. Huang, *Statistical mechanics*. New York: John Wiley & Sons, 1987.
- [6] G. A. Bird, *Molecular gas dynamics and the direct simulation of gas flows*. Oxford: Clarendon University Press, 1994.
- 370 [7] S. Chapman and T. G. Cowling, *The mathematical theory of non-uniform gases: an account of the kinetic theory of viscosity, thermal conduction and diffusion in gases*. Cambridge: Cambridge University Press, 3rd ed., 1970.
- [8] A. L. Garcia, J. Bell, W. Crutchfield, and B. Alder, “Adaptive mesh and algorithm refinement using Direct Simulation Monte Carlo,” *J. Comput. Phys.*, vol. 154, pp. 134–155, 1999.
- 375

- [9] M. M. Mansour, F. Baras, and A. Garcia, “On the validity of hydrodynamics in plane Poiseuille flows,” *Physica A*, vol. 240, pp. 255–267, 1997.
- 380 [10] W.-M. Zhang, G. Meng, and Z. Wei, “A review on slip models for gas microflows,” *Microfluid. Nanofluid.*, vol. 13, pp. 845–882, 2012.
- [11] H. Grad, “On the kinetic theory of rarefied gases,” *Commun. Pure Appl. Math.*, vol. 2, pp. 331–407, 1949.
- [12] H. Struchtrup, *Macroscopic transport equations for rarefied gas flows: Approximation methods in kinetic theory*. Heidelberg: Springer-Verlag, 2005.
- 385 [13] R. Roveda, D. B. Goldstein, and P. L. Varghese, “Hybrid Euler/particle approach for continuum/rarefied flows,” *J. Spacecraft Rockets*, vol. 35, pp. 258–265, 1998.
- [14] H. S. Wijesinghe, R. D. Hornung, A. L. Garcia, and N. G. Hadjiconstantinou, “Three-dimensional hybrid continuum-atomistic simulations for multiscale hydrodynamics,” *J. Fluids Eng.*, vol. 126, pp. 768–777, 2004.
- 390 [15] J.-S. Wu, Y.-Y. Lian, G. Cheng, R. P. Koomullil, and K.-C. Tseng, “Development and verification of a coupled DSMC-NS scheme using unstructured mesh,” *J. Comput. Phys.*, vol. 219, pp. 579–607, 2006.
- [16] T. E. Schwatzentruber, L. C. Scalabrin, and I. D. Boyd, “A modular particle continuum numerical method for hypersonic non-equilibrium gas flows,” *J. Comput. Phys.*, vol. 225, pp. 1159–1174, 2007.
- 395 [17] D. A. Kessler, E. S. Oran, and C. R. Kaplan, “Towards the development of a multiscale, multiphysics method for the simulation of rarefied gas flows,” *J. Fluid Mech.*, vol. 661, pp. 262–293, 2010.
- 400 [18] S. Pantazis and H. Rusche, “A hybrid continuum-particle solver for unsteady rarefied gas flows,” *Vacuum*, vol. 109, pp. 275–283, 2014.

- [19] K. Farber, P. Farber, J. Grabel, S. Krick, J. Reitz, and P. Ueberholz, “Development and validation of a coupled Navier-Stokes/DSMC simulation for rarefied gas flow in the production process for OLEDs.” In press, 2015.
- [20] J.-F. Bourgat, P. L. Tallec, and M. Tidriri, “Coupling Boltzmann and Navier-Stokes equations by friction,” *J. Comput. Phys.*, vol. 127, pp. 227–245, 1996.
- [21] P. L. Tallec and F. Mallinger, “Coupling Boltzmann and Navier-Stokes equations by half-fluxes,” *J. Comput. Phys.*, vol. 136, pp. 51–67, 1997.
- [22] A. L. Garcia and B. J. Alder, “Generation of the Chapman-Enskog distribution,” *J. Comput. Phys.*, vol. 140, pp. 66–70, 1998.
- [23] H. A. Al-Mohssen, N. G. Hadjiconstantinou, and I. G. Kevrekidis, “Acceleration methods for coarse-grained numerical solution of the Boltzmann equation,” *J. Fluids Eng.*, vol. 129, pp. 908–912, 2007.
- [24] P. Degond, J.-G. Liu, and L. Mieussens, “Macroscopic fluid models with localized kinetic upscaling effects,” *Multiscale Model. Simul.*, vol. 53, pp. 940–979, 2006.
- [25] S. Succi, “Mesoscopic modeling of slip motion at fluid-solid interfaces with heterogeneous catalysis,” *Phys. Rev. Lett.*, vol. 89, p. 064502, 2002.
- [26] F. Toschi and S. Succi, “Lattice Boltzmann method at finite Knudsen numbers,” *Europhys. Lett.*, vol. 69, pp. 549–555, 2005.
- [27] M. Sbragaglia and S. Succi, “Analytical calculation of slip flow in lattice Boltzmann models with kinetic boundary conditions,” *Phys. Fluids*, vol. 17, p. 093602, 2005.
- [28] M. Sbragaglia and S. Succi, “A note on the lattice Boltzmann method beyond the Chapman-Enskog limits,” *Europhys. Lett.*, vol. 73, pp. 370–376, 2006.

- [29] R. Zhang, Z. Shan, and H. Chen, “Efficient kinetic method for fluid simulation beyond the Navier-Stokes equation,” *Phys. Rev. E*, vol. 74, p. 046703, 2006.
- [30] S. Ansumali, I. V. Karlin, S. Arcidiacono, A. Abbas, and N. I. Pasiannakis, “Hydrodynamics beyond Navier-Stokes: exact solution to the lattice Boltzmann method,” *Phys. Rev. Lett.*, vol. 95, p. 260605, 2007.
- [31] X.-D. Niu, S.-A. Hyodo, T. Munekata, and K. Suga, “Kinetic lattice Boltzmann method for microscale gas flows: Issues on boundary condition, relaxation time, and regularization,” *Phys. Rev. E*, vol. 76, p. 036711, 2007.
- [32] G.-H. Tang, Y.-H. Zhang, and D. Emerson, “Lattice Boltzmann models for nonequilibrium gas flows,” *Phys. Rev. E*, vol. 77, p. 046701, 2008.
- [33] J. Meng and Y. Zhang, “Accuracy analysis of high-order lattice Boltzmann models for rarefied gas flows,” *J. Comput. Phys.*, vol. 230, pp. 835–849, 2011.
- [34] J. Meng and Y. Zhang, “Gauss-Hermite quadratures and accuracy of lattice Boltzmann models for nonequilibrium gas flows,” *Phys. Rev. E*, vol. 83, p. 036704, 2011.
- [35] T. Reis and P. Dellar, “Lattice Boltzmann simulations of pressure-driven flows in microchannels using Navier-Maxwell slip boundary conditions,” *Phys. Fluids*, vol. 24, p. 112001, 2012.
- [36] X. Liu and Z. Guo, “A lattice Boltzmann study of gas flows in a long micro-channel,” *Comput. Math. Appl.*, vol. 65, pp. 186–193, 2013.
- [37] S. Tao and Z. Guo, “Boundary condition for lattice Boltzmann modeling of microscale gas flows with curved walls in the slip regime,” *Phys. Rev. E*, vol. 91, p. 043305, 2015.
- [38] S. Succi, *The Lattice Boltzmann Equation for fluid dynamics and beyond*. Oxford: Clarendon University Press, 2001.

- [39] J. Zhang, “Lattice Boltzmann method for microfluidics: models and applications,” *Microfluid. Nanofluid.*, vol. 10, pp. 1–28, 2011.
- [40] F. Verhaeghe, L.-S. Luo, and B. Blanpain, “Lattice Boltzmann modeling of microchannel flow in slip flow regime,” *J. Comput. Phys.*, vol. 228, pp. 147–157, 2009.
- [41] Z. Guo, J. Qin, and C. Zheng, “Generalized second-order slip boundary condition for nonequilibrium gas flows,” *Phys. Rev. E*, vol. 89, p. 013201, 2014.
- [42] S. Ansumali and I. V. Karlin, “Kinetic boundary conditions in the lattice Boltzmann method,” *Phys. Rev. E*, vol. 66, p. 026311, 2002.
- [43] Z. Chai, Z. Guo, L. Zheng, and B. Shi, “Lattice Boltzmann simulation of surface roughness effect on gaseous flow in a microchannel,” *J. Appl. Phys.*, vol. 104, p. 014902, 2008.
- [44] X. Shan, X.-F. Yuan, and H. Chen, “Kinetic theory representation of hydrodynamics: a way beyond the Navier-Stokes equation,” *J. Fluid Mech.*, vol. 550, pp. 413–331, 2006.
- [45] A. Montessori, M. L. Rocca, G. Falcucci, and S. Succi, “Regularized lattice BGK versus highly accurate spectral methods for cavity flow simulations,” *Int. J. Mod. Phys. C*, vol. 25, p. 1441003, 2014.
- [46] G. H. Tang, W. Q. Tao, and Y. L. He, “Lattice Boltzmann method for gaseous microflows using kinetic theory boundary conditions,” *Phys. Fluids*, vol. 17, p. 058101, 2005.
- [47] G. H. Tang, Y. H. Zhang, X. J. Gu, and D. R. Emerson, “Lattice Boltzmann modelling Knudsen layer effect in non-equilibrium flows,” *Europhys. Lett.*, vol. 83, p. 40008, 2008.
- [48] M. A. Gallis, J. R. Torczynski, D. J. Rader, M. Tij, and A. Santos, “Normal solutions of the Boltzmann equation for highly nonequilibrium Fourier flow and Couette flow,” *Phys. Fluids*, vol. 18, p. 017104, 2006.

- [49] C. R. Lilley and J. E. Sader, “Velocity profile in the Knudsen layer according to the Boltzmann equation,” *Proc. R. Soc. A*, vol. 464, pp. 2015–2035, 2008.
- [50] X. Shan, “General solution of lattices for cartesian lattice Bhatnagar-Gross-Krook models,” *Phys. Rev. E*, vol. 81, p. 036702, 2010.
- [51] C. R. Kaplan and E. S. Oran, “Nonlinear filtering for low-velocity gaseous microflows,” *AIP Conference Proceedings*, vol. 585, pp. 472–479, 2001.
- [52] J. Fan and C. Shen, “Statistical simulation of low-speed rarefied gas flows,” *J. Comput. Phys.*, vol. 167, pp. 393–412, 2001.
- [53] L. L. Baker and N. G. Hadjiconstantinou, “Variance reduction for Monte Carlo solutions of the Boltzmann equation,” *Phys. Fluids*, vol. 17, p. 051703, 2005.
- [54] N. G. Hadjiconstantinou, A. L. Garcia, M. Z. Bazant, and G. He, “Statistical error in particle simulations of hydrodynamic phenomena,” *J. Comput. Phys.*, vol. 187, pp. 274–297, 2003.